



**HAL**  
open science

## Etching of m-plane Zn(Mg)O epitaxial films and its impact on surface leakage currents

Borislav Hinkov, Hanh Hoang, Maxime Hugues, Jean-Michel Chauveau, Gottfried Strasser

► **To cite this version:**

Borislav Hinkov, Hanh Hoang, Maxime Hugues, Jean-Michel Chauveau, Gottfried Strasser. Etching of m-plane Zn(Mg)O epitaxial films and its impact on surface leakage currents. *Semiconductor Science and Technology*, 2021, 36 (3), pp.035023. 10.1088/1361-6641/abdd07 . hal-03423387

**HAL Id: hal-03423387**

**<https://hal.science/hal-03423387>**

Submitted on 22 Nov 2021

**HAL** is a multi-disciplinary open access archive for the deposit and dissemination of scientific research documents, whether they are published or not. The documents may come from teaching and research institutions in France or abroad, or from public or private research centers.

L'archive ouverte pluridisciplinaire **HAL**, est destinée au dépôt et à la diffusion de documents scientifiques de niveau recherche, publiés ou non, émanant des établissements d'enseignement et de recherche français ou étrangers, des laboratoires publics ou privés.

PAPER • OPEN ACCESS

## Etching of *m*-plane Zn(Mg)O epitaxial films and its impact on surface leakage currents

To cite this article: Borislav Hinkov *et al* 2021 *Semicond. Sci. Technol.* **36** 035023

View the [article online](#) for updates and enhancements.



**The Electrochemical Society**  
Advancing solid state & electrochemical science & technology

The ECS is seeking candidates to serve as the  
**Founding Editor-in-Chief (EIC) of ECS Sensors Plus,**  
a journal in the process of being launched in 2021

The goal of ECS Sensors Plus, as a one-stop shop journal for sensors, is to advance the fundamental science and understanding of sensors and detection technologies for efficient monitoring and control of industrial processes and the environment, and improving quality of life and human health.

*Nomination submission begins: May 18, 2021*



Nominate now!

# Etching of *m*-plane Zn(Mg)O epitaxial films and its impact on surface leakage currents

Borislav Hinkov<sup>1</sup> , Hanh T Hoang<sup>1</sup> , Maxime Hugues<sup>2</sup>, Jean-Michel Chaveau<sup>2</sup> and Gottfried Strasser<sup>1</sup> 

<sup>1</sup> Institute of Solid State Electronics & Center for Micro- and Nanostructures, Technische Universität (TU) Wien, 1040 Vienna, Austria

<sup>2</sup> Université Côte d'Azur, CNRS, CRHEA, 06560 Valbonne, France

E-mail: [borislav.hinkov@tuwien.ac.at](mailto:borislav.hinkov@tuwien.ac.at)

Received 12 October 2020, revised 29 December 2020

Accepted for publication 18 January 2021

Published 24 February 2021



## Abstract

Zinc oxide is a novel material system for mid-infrared and THz optoelectronics. Especially its non-polar *m*-plane orientation is a promising candidate for the design of devices like quantum cascade lasers (QCLs) and detectors (QCDs). But for their realization novel fabrication schemes are needed. We present a new inductively coupled plasma reactive ion etching (ICP-RIE) process for etching of *m*-Zn(Mg)O heterostructures in a CH<sub>4</sub>-based chemistry. The process has been optimized for smooth vertical sidewalls together with high selectivity towards a SiN etch mask. This was achieved by combining the RIE etching with wet chemical etching in strongly diluted HCl. Similar to various types of semiconductor-based optoelectronic materials and devices (Sidor *et al* 2016 *J. Electron. Mater.* **45** 4663–7; Ma *et al* 2016 *Opt. Express* **24** 7823), including other wide-gap semiconductors like (In)GaN (Zhang *et al* 2015 *Nanotechnology* **26**), we observe surface leakage currents in etched *m*-plane Zn(Mg)O structures. We show that they depend on the applied etching process and surface treatment techniques as well as the barrier composition in the Zn(Mg)O heterostructures. In addition, a treatment in hydrogen peroxide (H<sub>2</sub>O<sub>2</sub>) yields a significant surface leakage current suppression up to several orders of magnitude.

Supplementary material for this article is available [online](#)

Keywords: optoelectronics, widegap semiconductors, intersubband physics, quantum cascade laser, semiconductor processing, II–VI semiconductors

## 1. Introduction

The terahertz (THz) spectral region is a peculiar portion of the electromagnetic spectrum. It is sandwiched between the mid-infrared and the microwave spectral range and often

referred to as ‘the THz gap region’, because of its lack of high performance coherent light sources like compact semiconductor lasers. At the same time, it is relevant for a wide variety of applications ranging from trace gas sensing and medical diagnostics [4–6] to spectral imaging and detection in the THz [7–10], astronomical measurements (including space-born species detection) [11, 12] and security (screening) applications [13]. Unfortunately, the lack of suitable high-performance THz lasers operating at or at least close to room temperature, prevents addressing those applications appropriately and limits the usability of already existing devices significantly.



Original Content from this work may be used under the terms of the [Creative Commons Attribution 4.0 licence](#). Any further distribution of this work must maintain attribution to the author(s) and the title of the work, journal citation and DOI.

The difficulties in the development of semiconductor-based THz lasers can be shown best, by the progress of the currently most promising candidate for such devices: the THz quantum cascade laser (QCL). THz QCLs were demonstrated for the first time in 2002 by [14]. But even with putting significant effort into the development for the following almost two decades and using the very mature material system of GaAs, THz QCLs could only recently show lasing operation on a very powerful thermoelectric cooler [15] and up to 210 K [16]. Therefore, room temperature operation is still out of reach for GaAs-based THz QCLs.

One of the major limitations in GaAs-based THz devices arises from the materials relatively low longitudinal-optical (LO)-phonon energy of 36 meV (see e.g. [17]), which is on the same order as the corresponding optical THz transitions ( $\sim 4$ –41 meV). Together with the long radiative intersubband (ISB) lifetimes in the THz spectral range being in strong competition with the very efficient non-radiative LO-phonons and their shorter lifetimes [18], it makes laser operation very inefficient. In addition to the previously mentioned difficulties, increasing the device temperature towards room temperature ( $\sim 300$  K), makes those problems become even more severe, since the thermal energy at room temperature ( $kT \sim 26$  meV) is on the same order as the LO-phonon energy ( $E_{\text{LO,GaAs}} = 36$  meV). Consequently, there is a need for disruptive new approaches, e.g. by using novel material systems with higher LO-phonon energies like GaN ( $E_{\text{LO,GaN}} = 96$  meV) or ZnO ( $E_{\text{LO,ZnO}} = 72$  meV).

Alternative material systems have already been tested for their suitability for THz emitting QCLs in the past. This includes InAs- and InP-based [19–22] as well as GaN-based devices [23, 24]. While the former have resulted in operational THz QCLs with decent performance (InAs- [25] and InP-based [21] THz QCLs have a higher peak material gain than GaAs devices [25, 26] due to a lower effective electron mass), they are still limited to cryogenic temperatures [22, 27], also due to their low LO phonon energies ( $E_{\text{LO,InAs}} = 29$  meV [28],  $E_{\text{LO,InP}} = 43$  meV [29]) which are comparable to  $E_{\text{LO,GaAs}} = 36$  meV. In comparison to that, the GaN material system could also reach lasing operation. But while it even extended the accessible wavelength range to higher frequencies of 5.5 and 7 THz [23], it yet left the predicted room temperature operation [24] out of reach [30, 31].

We therefore propose to use ZnO as suitable alternative material system for optoelectronic devices like (THz) QCLs and quantum cascade detectors (QCDs), owing to its high LO phonon energy mentioned previously. It is also predicted that such devices allow THz QCL emission up to above room temperature [32]. Hereby, ZnO is in general a relatively new optoelectronic material, in particular its application in the THz spectral range. Hence, significant effort has to be put in the characterization and analysis of its material parameters in the THz, like e.g. the effective mass and permittivity, as well as its electronic band parameters like the conduction band offset. These efforts also include mastering its high-quality epitaxial growth and the development of state-of-the-art device fabrication schemes.

To date, ZnO [33] has been and still is mainly used in the rubber (about 50%–60%) and ceramics industry [34], only to minor extent exploiting its functional material properties [35] through e.g. UV optoelectronic [36] and photovoltaic [37, 38] devices as well as transparent electronics [39] and sensing applications [40]. But no significant effort was put so far to enable its full potential towards ISB physics and device applications, especially in the THz spectral range. Like GaN, ZnO is a polar material (its main conformation is the wurtzite lattice [33, 41]), resulting in the formation of internal electric polarization fields [42] for its main crystallographic directions like the c-plane orientation (0001). This strongly increases the difficulty of designing and realizing complex ISB devices like QCLs or QCDs with their up to hundreds of precisely designed quantum wells. Thus, it is highly beneficial to use a *non-polar* crystallographic orientation like the a-plane ( $2\bar{1}\bar{1}0$ ) or the m-plane (01 $\bar{1}0$ ) direction [43, 44], which yield no internal fields.

While the epitaxial growth of high-quality *m-plane* ZnO layers with up to monolayer precision could be realized in the past [45–48], ISB absorptions at room temperature [49, 50] or the realization of room temperature (mid-infrared) QCDs [51], could just recently be demonstrated in m-plane Zn(Mg)O devices.

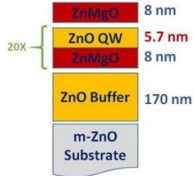
In this paper we give detailed instructions and show results on the fabrication of such m-plane Zn(Mg)O devices. The main focus will lie on the etching procedure of ZnO/ZnMgO heterostructures down to nanometer precision. We developed a novel combined etching scheme including a first step of plasma-based dry etching in a reactive ion etching (RIE) machine, followed by a wet chemical (smoothing) etch and a final step of surface passivation to prevent surface leakage currents (similar as known from GaN based devices, e.g. [3]). The whole etching procedure is optimized for smooth vertical sidewall profiles together with a high selectivity towards the etching mask and also high, while still well-controllable, etch rates.

## 2. Samples

The samples analyzed in this work are grown by molecular beam epitaxy (MBE) on a  $3 \times 2$  inch ‘Riber EPINEAT’ system on non-polar m-plane ZnO substrates (mainly from the company ‘Crystec’), to prevent the formation of internal electrical fields. We use ZnO as quantum well material together with ZnMgO as barriers with varying Mg-content (typically between 10% and 30%). The active region and contact layers are n-doped with Gallium, typically between  $5 \times 10^{17} \text{ cm}^{-3}$  and  $\sim 10^{20} \text{ cm}^{-3}$ .

In order to be able to etch a wide variety of different ZnO-based samples, the etchings were tested and optimized for various Zn(Mg)O layer sequences ranging from bare m-plane ZnO substrates (350–500  $\mu\text{m}$ ) to additional hundreds of nanometer thick epitaxial layers, including heterostructures with only a few nanometer thick individual layers, as known from QCLs and QCDs. In addition, we also varied the total etch depth from some 10 nm only up to about 10  $\mu\text{m}$ .

**Table 1.** Display of four different samples on m-plane ZnO substrate, used in the etch tests for CH<sub>4</sub>-based dry (see detailed recipe below) and HCl-based wet chemical etching (*by column*): 1. bare substrate, 2. 1 μm epitaxial ZnO, 3. 283 nm multi-quantum-well (mQW) on 170 nm ZnO buffer and 4. 150 nm ZnMgO. The etch rates are given in row 4–6.

	ZnO substrate	ZnO (doped)	ZnO/Zn <sub>0.77</sub> Mg <sub>0.23</sub> O mQW	Zn <sub>0.77</sub> Mg <sub>0.23</sub> O
Layer sequence				
Epitaxial layer thickness	—	1 μm	283 nm (mQW) + 170 (ZnO buffer)	150 nm
RIE etching rate (nm min <sup>-1</sup> )	42	49	33	35
HCl etching rate (1:4) (nm s <sup>-1</sup> )	29.2	43.2	26.1	19.9
HCl etching rate (1:16) (nm s <sup>-1</sup> )	22.6	17	6.9	4.4

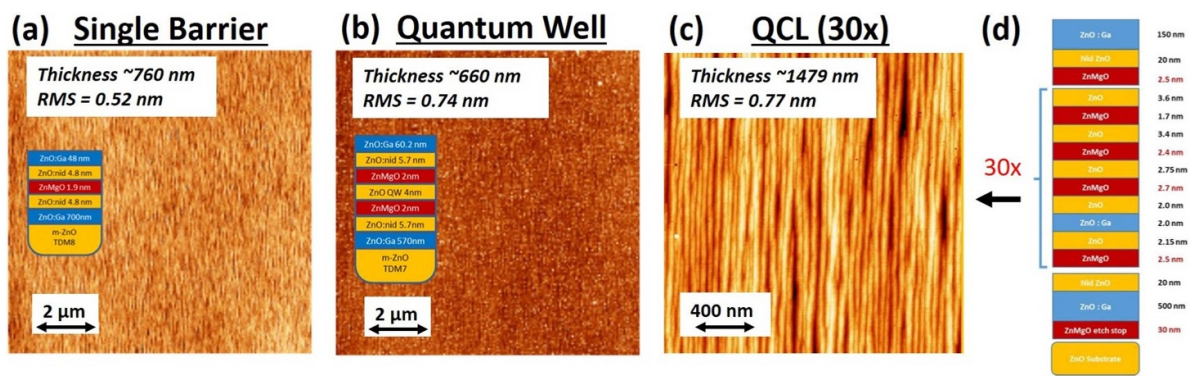


**Figure 1.** AFM measurements of MBE-grown structures on m-plane ZnO substrate with increasing number of layers and therefore complexity: (a) ZnMgO single barrier, (b) ZnO/ZnMgO single quantum well and (c) ZnO/ZnMgO-based QCL structure with 30 periods. (d) One period of a typical QCL layer sequence (corresponding AFM shown in (c)).

Table 1 shows the detailed layer sequences which were used to test the final etch recipes (dry and wet etching), ordered by decreasing etched ZnO thickness. Besides the first sample, which is a bare substrate, all other consist of MBE grown layers of ZnO and/or ZnMgO. Their individual total epitaxial layer thickness is given in the second row. For better comparison, the Mg-content is kept constant for the given samples. The different etch-rates will be discussed in detail later on in section 3.5.

Figure 1 shows AFM measurements of typical epitaxial layers after MBE growth, with increasing number of layers and thus complexity. All structures are sandwiched between ZnO contact layers.

The total grown layer thicknesses are ~760 nm, ~660 nm and ~1479 nm for figures 1(a)–(c), respectively. The detailed layer sequence is given in the individual insets (figures 1(a) and (b)) and in figure 1(d) for figure 1(c).

The surface quality, defined by its RMS roughness, yields increasing values of figure 1(a) 0.52 nm, (b) 0.74 nm and (d) 0.77 nm, respectively, as the number of grown layers increases. These values are on the same order as published in literature: e.g. RMS = 0.385 nm [41]. But the latter

where measured on *as-grown* o-polar (000 $\bar{1}$ ) single-crystalline epi-ready substrates (*Crystec*) without any additional epitaxial growth or other deposition. Thus, the obtained values from the present work confirm the high quality of the epitaxial growth. It is worth noting, that a preferred direction of ‘roughness’ can be distinguished in our samples. While in the vertical direction, individual ‘lines’ can be identified, which barely show any roughness, the opposite is true for the horizontal direction. Abrupt changes in height as function of the measured position, i.e. a surface roughness, is observed. Such a preferred orientation of the surface roughness can be well identified in figure 1(c). It is less pronounced in figures 1(a) and (b), but can still be identified (attention to different scaling).

### 3. Etching of m-plane Zn(Mg)O

Etching of semiconductors can be performed utilizing different techniques out of which *wet* chemical etching and *dry* etching in a plasma reactor, are the most widely used ones. For fabricating optical waveguides, which are one key component for optoelectronic devices, the important characteristics are:

smooth (on the wavelength-scale of the device) and vertical sidewalls together with a good surface quality after etching. Consequently, the following process parameters are beneficial: a good selectivity towards the etching mask, a relatively high etch rate for micrometer-scale etching and a preferably anisotropic etching to prevent a strong undercut under the photomask together with vertical sidewalls. For this study, we tested both types, dry and wet etching, of *m*-plane Zn(Mg)O-based samples, in our lab, including different wet etching solutions and various inductively coupled plasma reactive ion etching (ICP-RIE) dry etching recipes.

### 3.1. Wet chemical etching of *m*-plane Zn(Mg)O epitaxial layers

While the ZnO material system with its various crystallographic orientations (*c*-, *m*-, *a*-, *r*-plane etc) is etched by a wide variety of liquids including typical *acidic* and *alkaline* solutions like HCl [52–54], (CH<sub>3</sub>COOH):H<sub>3</sub>PO<sub>4</sub> [41, 52] or HNO<sub>3</sub> [52] and NaOH [55–57] or KOH [53, 58, 59], respectively, their characteristics and thus also resulting etch profiles vary significantly.

As revealed by wet chemical etching, an in-plane anisotropy of the crystalline structure results in different etch rates for the individual crystalline directions (see e.g. different etch rates for (11 $\bar{2}$ 0) Zn(Mg)O samples on *r*-plane (01 $\bar{1}$ 2) Al<sub>2</sub>O<sub>3</sub> substrates, when comparing etching of the in-plane (*c*-axis (0001)) and its perpendicular (1 $\bar{1}$ 00) direction [36, 60]). We observe and present a similar anisotropic effect in *m*-plane (01 $\bar{1}$ 0) Zn(Mg)O samples. In addition, it is noteworthy, that *m*-plane ZnO yields different etching characteristics compared to previously analyzed *a*- or *c*-ZnO samples [61].

Knowing the total etched layer thickness together with the needed etching precision is an important pre-requisite to determine well-controllable etch-rates resulting from the dilution of the etchant. In (MIR-/THz-)QCLs and QCDs we typically have to etch between tens of nanometers up to  $\sim 10 \mu\text{m}$ , while the thickness of the targeted contact layers lies between  $\sim 50$  and  $300 \text{ nm}$ .

Testing four different etchants for different dilutions in DI water: HCl(32%), H<sub>3</sub>PO<sub>4</sub>(85%), CH<sub>3</sub>COOH(96%):H<sub>3</sub>PO<sub>4</sub>(85%) and HNO<sub>3</sub>(65%), we obtain high etch rates (several micrometers/minute) and selectivity (sputtered gold or PECVD-deposited SiN hardmask are not etched), which are clearly very beneficial characteristics. In contrast to that, the resulting etch profiles are typically trapezoidal sloped, together with a more or less pronounced undercut, i.e. *lateral* etching, under the etch mask, which can create problems during further device fabrication. More details including particular etch rates and images of the etch profiles are given in section 8.1 of the supplementary material (available online at [stacks.iop.org/SST/36/035023/mmedia](https://stacks.iop.org/SST/36/035023/mmedia)).

### 3.2. ICP-RIE etching of *m*-plane Zn(Mg)O epitaxial layers

ICP-RIE is a widely used etching technique, which can lead to enhanced etching profiles, i.e. significantly lower undercut

under the etch mask. This can be achieved through better control of the previously mentioned in-plane etching anisotropy, by carefully adjusting the process parameters. Moreover, ICP-RIE can often provide better control on the etch depths, due to moderate etch rates in combination with very precise control on etching parameters like gas flow rates, temperature and applied RF-bias.

In addition to a chemical etching component as in wet chemical etching, ICP-RIE processes rely on physical etching processes from ‘bombarding’ the sample surface with accelerated ions like ionized Ar atoms. This *physical* removal process is crucial for: (a) breaking the bonds of the constituents of the etched semiconductor lattice and (b) efficiently removing etch by-products from the sample surface. The former: (a) is important in ZnO due to the high Zn to O chemical bonding strength (see x-ray photon spectroscopy (XPS) measurements of as-grown ZnO films: binding energy  $\cong 1045 \text{ eV}$  (Zn 2p<sub>1/2</sub>) and  $1022 \text{ eV}$  (Zn 2p<sub>3/2</sub>) [62]) and the latter: (b) for the low vapor pressure of the etch by-products in ZnO [63–65]. In addition, it has to be well-adjusted through carefully balancing RF- and ICP-power, to minimize surface damage effects.

In our study, we focus on two different gas mixtures and their suitability to etch *m*-plane ZnO: SiCl<sub>4</sub>(/Ar) and CH<sub>4</sub>/H<sub>2</sub>(/Ar). Both have previously been used to etch other types of ZnO samples and devices already, see e.g.: [41, 60, 63, 66–69] and the supplementary material section 8.2 for more details on the ICP-RIE process in ZnO.

The availability of SiCl<sub>4</sub> and CH<sub>4</sub>/H<sub>2</sub> together with Ar within our ICP-RIE reactor ‘Oxford Plasmalab 100’, allowed us to perform the first comparative study between chlorine- and methane-based etching of epitaxially grown *m*-plane Zn(Mg)O.

### 3.3. SiCl<sub>4</sub>-based etching of *m*-plane ZnO

Chlorine-based ZnO etching has so far mainly been used in the two chemistries Cl<sub>2</sub>(/Ar) [64, 65] and SiCl<sub>4</sub>(/Ar) [41, 60, 67]. While the former shows relatively fast etch rates between  $50 \text{ nm min}^{-1}$  and  $206 \text{ nm min}^{-1}$  [64, 65], the selectivity towards a photoresist (PR) etch mask is very poor ( $\leq 0.34 \rightarrow$  resist etched  $\sim 3\times$  faster than ZnO [65]). This is a direct consequence of the high bias voltages of  $V_{\text{dc}} > 250 \text{ V}$ , needed for desorption of the low-vapor-pressure ZnCl<sub>2</sub> etch by-product.

In contrast to that, SiCl<sub>4</sub>(/Ar) etches significantly slower in the range of  $\sim 5 \text{ nm min}^{-1}$  up to  $\sim 37.5 \text{ nm min}^{-1}$  [60, 67, 70], while the selectivity was not specifically analyzed so far.

In order to avoid poor selectivity and other negative effects (see 8.3), the tests in our study have been conducted using a sputtered Au-mask. We varied the SiCl<sub>4</sub>/Ar gas flow as well as RF- and ICP-power at room-temperature and analyzed the obtained etch-rate, selectivity and etch-profile for low chamber pressure ( $\leq 20 \text{ mTorr}$ ), i.e. in a rather diluted plasma. The best etching is given by SiCl<sub>4</sub>:Ar (30:0 sccm) at  $20 \text{ mTorr}$  and RF- : ICP-power (50 W : 200 W) which results in an etch-rate of  $\sim 12 \text{ nm min}^{-1}$  and a selectivity of 2:1 (ZnO: Au-mask). Further details, including etch-profile and other tested recipes for this chemistry, are given in the supplementary material section 8.3 and supplementary figure 6.

We can conclude, that our etch-rates are in the same range as in literature for other types of ZnO samples [60, 67, 70]. Our etch profiles are vertical for all tested parameters (see supplementary figure 6) and only show slightly positively sloped sidewalls for a very high partial Ar pressure (5 sccm : 40 sccm (SiCl<sub>4</sub>:Ar), *SIA*). This is also in good agreement with findings from literature for chlorine-based etching: e.g.  $\leq 70^\circ\text{C}$  [65].

Nevertheless, the suitability of SiCl<sub>4</sub>-based etching for m-ZnO optoelectronic devices is limited twofold: firstly, due to the very low etch-rate, limiting etching micrometer thick layers ( $10\ \mu\text{m} \cong 16\ \text{h}$ ) and secondly, due to the poor selectivity even towards a sputtered Au-mask (best case: 2:1 for ZnO:Au-mask). The poor selectivity is also an issue when using alternatives like e.g. PR-masks, while other metal-based masks like Cr/Ni are difficult to be removed without damaging the ZnO [60, 65].

### 3.4. CH<sub>4</sub>-based etching of m-plane Zn(Mg)O

The reaction of ZnO with CH<sub>x</sub> radicals leads to higher etch-rates as compared to SiCl<sub>4</sub>-based etching, due to the favorable, i.e. higher, etch by-product vapor pressure [63]. As shown e.g. by [68], the CH<sub>4</sub>-based etch-rate strongly depends on and increases with the ratio *R* of its chemical component CH<sub>4</sub>, as part of the total gas-composition, i.e.  $R = \frac{\text{CH}_4[\text{sccm}]}{\text{CH}_4 + \text{H}_2(+\text{Ar})[\text{sccm}]}$ . Hereby, the investigated range in literature covers extremely low CH<sub>4</sub>-concentrations of  $R = 0.044$  [71] and  $0.05$  [72] only, up to high values of  $R = 0.6$  [68],  $0.66$  [63] and  $0.74$  [70], respectively. Additional parameters that determine the amount of chemical and physical etching are given by the applied RF-power, the chamber pressure and, if available at the plasma reactor, the applied ICP-power. For more details and a more detailed comparison to literature see table 3 in the supplementary material section 8.4.

To reduce sample surface and also mask damage, we developed a novel etching recipe with strong chemical contribution with higher selectivity and still high enough etch-rates ( $\gg 30\ \text{nm}\ \text{min}^{-1}$ ), while applying just as much physical sputtering as necessary. After thorough testing and characterization, we came up with the following recipe: a very high methane content of  $R = 0.83$  is combined with a strong RF-power of 250 W ( $\approx 450\text{--}500\ \text{V}$ ) and ICP-power of 200 W. Both add to the needed physical sputtering to break the Zn to O bonds and additionally, remove any etch by-products during the etching-process. In addition to that, the chamber pressure is kept very low for a diluted plasma (20 mTorr) and the temperature is fixed at  $25^\circ\text{C}$ . It is interesting to note, that changing the temperature to e.g.  $100^\circ\text{C}$  has barely any influence on the etch-rate of our recipe. More details are shown in in the first row of supplementary table 3.

While only a few previous studies analyze the selectivity of CH<sub>4</sub>-etching towards the etch-mask (see e.g. [69] for PMMA resist or [68] for regular PR), none performed a comparison for different mask materials. It is important since it distinguishes parameters as maximum etch-depth and impacts on the obtained etch profile including sidewall defect density, which e.g. add to the waveguide losses in an optical waveguide

and therefore increase the lasing threshold of corresponding devices [18, 73].

We performed a detailed analysis and tested PR (=  $1.4\ \mu\text{m}$ , type: AZ 5214E), Au (=  $1\ \mu\text{m}$ , sputtered) and SiN (=  $1.3\ \mu\text{m}$ , PECVD) as mask material. It includes their deposition and a comparison of prior to and after etching, which is shown in supplementary figure 7. While all details of this analysis are given in the supplementary material section 8.4, the main results are also shown in figure 2 and described in the following.

Figure 2 shows SEM-based topview pictures for the three tested masks after etching: (a+b) PR (thickness:  $d_{\text{prior}} = 1.4\ \mu\text{m}$ , etched ZnO =  $4\ \mu\text{m}$ ), (c) Au ( $d_{\text{prior}} = 1\ \mu\text{m}$ , etched ZnO =  $1.7\ \mu\text{m}$ ) and (d) SiN ( $d_{\text{prior}} = 1.3\ \mu\text{m}$ , etched ZnO =  $1.7\ \mu\text{m}$ ). While the sample in figure 2(a) is still with the etching mask, this is not the case for (b)–(d).

After the methane-based etching, the results with the three masks are very different. While effectively etching the PR sample by about  $4\ \mu\text{m}$ , measured after safely removing the PR mask in acetone, which is not attacking the ZnO or ZnO/ZnMgO heterostructures underneath, we can see in figure 2(a), that the PR ‘blows up’ in some parts due to too much local heating or instead in other parts gets completely removed. Figure 2(b) reveals that the resulting sidewalls are very rough and not straight at all but rather sloped.

In contrast to that, the obtained sidewalls when etching  $1.7\ \mu\text{m}$  of ZnO with a Au-mask are pretty smooth and only gradually more rough than prior to etching (cp. figures 7(b) and (f)). Unfortunately, parts of the Au mask get re-sputtered during the etching process onto the sample, especially along the etched ZnO sidewall (see figure 2(c)) and partially even remain on top after removing the remainders of the Au mask with a quick dip in KI/I<sub>2</sub> (not damaging the ZnO or ZnO/ZnMgO heterostructures underneath). Therefore, Au is also not suitable to be used as mask material under these conditions, since the Au ‘contamination’ after etching is difficult to be removed.

Finally, we analyzed SiN for its suitability as etch-mask. As figure 2(d) reveals, the sidewalls after etching are absolutely vertical (confirmation for etch by-products only volatile in an ion assisted process [64]) and the ‘roughness’ on the hundreds of nanometer scale is directly transferred from the SiN-mask prior to etching into the etched ZnO. Another very pronounced feature can also be observed in figure 2(d): the occurrence of high-density pyramid-shaped and ‘grass-like’ structures. They most likely either result from a non-equiangular removal of Zn and O and their etch by-products [64] or originate from threading dislocations and surface defects, well known to wurtzite semiconductors, which lead to the formation of typically hexagonal textures after crystallographic-orientation dependent etching [41]. Since all three test samples showed the same surface prior to etching, we believe that the ‘grass’ originates from varying Zn- and O- etch-rates, rather than the sample surface prior to etching (the other samples did not show any similar behavior after etching and also additional TEM measurements did not reveal any threading dislocations prior to etching, thus disagreeing with this theory).

In addition to that, we also investigated several techniques for removing SiN from a ZnO surface. We found that etching

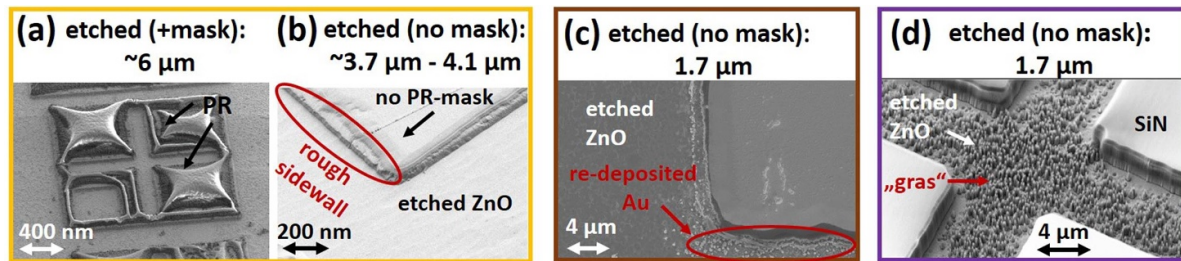


**Figure 2.** SEM topview images of three different masks for CH<sub>4</sub>-based ZnO etching: (a) and (b) PR AZ 5214E, (c) sputtered Au, (d) PECVD SiN. While the used etching mask is still on top of the sample in (a), this is not the case for samples (b)–(d).

SiN in a RIE-reactor either in a CHF<sub>3</sub>/O<sub>2</sub>-based or a SF<sub>6</sub>-based plasma has at most minimal impact on a ZnO surface underneath the SiN, i.e. the surface is etched at maximum a few nanometers with no observable additional damage.

In conclusion, even though the PR-mask (AZ 5214E) is very promising and PR has already been used successfully in literature for methane-based etching including very high selectivity [68], it is not suitable in our case due to the destruction of the PR while etching. The sputtered Au-mask sample is excluded because it suffers from Au re-deposition on the sample surface which is difficult to be removed or at least controlled.

In contrast to that, the SiN sample which reveals pyramidally-shaped structures can be ‘smoothed’ on its surface by an additional wet-etching step, as tested before in section 3.1 and will be discussed in the next section of this manuscript. More details on the CH<sub>4</sub> etching can be found in the supplementary material section 8.4.

### 3.5. Combined dry and wet etching for ZnO-based optoelectronic devices

As presented in section 3.1, multiple wet etchants were tested in this study. HCl was identified as the most suitable one for our m-plane ZnO samples. Thus it was also tested for removing the grass-like pyramids and smoothing the ‘pointy edges’ in the sidewalls after the methane-based RIE-etching (see section 3.4). Figure 3 shows SEM images of the whole etching procedure, which consists of: (a) masking of the ZnO sample with patterned SiN (fabrication as described in the supplementary material section 8.4), (b) dry-etching of the ZnO in the methane-based ICP-RIE plasma (see section 3.4) and (c) wet-etching of the sample in a strongly diluted HCl solution (HCl/H<sub>2</sub>O : 1/16). The SEM images of figure 3(c) reveal, that the HCl etching is a very good procedure to get rid of the grass-like defects as well as any sidewall-roughness, including pointy defects. The resulting sidewalls are almost perfectly vertical and smooth, while the plain ZnO is flat and smooth with barely any remaining surface roughness.

Consequently, the shown ZnO patterning procedure is a well-suitable way to fabricate waveguide-structures into epitaxially grown (single-crystal) m-plane ZnO layers yielding minimal sidewall and surface roughness. In a next step, we want to analyze the etching of ZnO/ZnMgO heterostructures, since they are the main building-block for our ZnO-based

quantum devices. Especially, any difference in the etch rate for those two materials is of particular interest and will be investigated.

### 3.6. Selectivity of m-plane ZnO vs ZnMgO etching and the usability as etch stop layer

The sample characteristics presented in the previous sections, were solely based on m-plane ZnO substrates. To ensure reliability and reproducibility of the results and avoid artifacts originating from a defective initial sample surface, we exclusively used so-called ‘epi-ready’ substrates, i.e. substrates, where the surface is prepared for an epitaxial growth. Similar to ZnO, the etching characteristics of ZnMgO vary and depend on the actual sample-type, layer composition and sequence and the applied etching mechanism itself. Literature shows e.g. that while HCl etching leads to dilution-dependent selective etching of ZnO ( $\text{ZnO}(\text{conc}_M) = 1 \times 10^{-2} - 1.2 \text{ M} \Rightarrow \text{etch-rate} = \sim 1 - 53 \text{ nm min}^{-1}$ ) versus Zn<sub>0.9</sub>Mg<sub>0.1</sub>O ( $\text{Zn}_{0.9}\text{Mg}_{0.1}\text{O}(\text{conc}_M) = 6 \times 10^{-3} - 2.4 \times 10^{-2} \text{ M} \Rightarrow \text{etch-rate} = \sim 350 - 1150 \text{ nm min}^{-1}$ ), with ZnMgO etching much faster [61], the opposite is the case for etching in a SiCl<sub>4</sub> plasma [60].

The slower ZnMgO etching in the latter case can be explained through the lower vapor pressure of the etch by-product MgCl<sub>2</sub> for ZnMgO etching [60] as compared to ZnCl<sub>2</sub> for ZnO etching [63, 64]. This result is in strong contrast to the HCl etching, i.e. ZnMgO being etched much faster ( $\sim 5 - 6$  times).

Such a difference in the etch-rate is, on one hand, important to be controlled when etching heterostructures (see e.g. ‘fishbone-like’ etching structures in InGaAs/AlInAs QCLs [74]), but can also be beneficial since it enables the use of certain materials/compositions as etch-stop layers. They are e.g. needed in the fabrication of so called double-metal waveguides for THz-QCLs [75–77].

Table 1 reveals different etch-rates for wet (HCl-) as well as dry (CH<sub>4</sub>-)based etching of m-plane: (a) ZnO substrate, (b) doped ZnO (MBE-grown), (c) ZnO/Zn<sub>0.77</sub>Mg<sub>0.23</sub>O heterostructure (MBE-grown) and (d) Zn<sub>0.77</sub>Mg<sub>0.23</sub>O. While CH<sub>4</sub>-based ICP-etching shows up to 48% faster etching compared to ZnMgO, the difference is not large enough for surface planarization. The situation is different for HCl-etching (dilution: 1:16), for which the selectivity ZnO/ZnMgO reaches values of >5 (see also table 2).

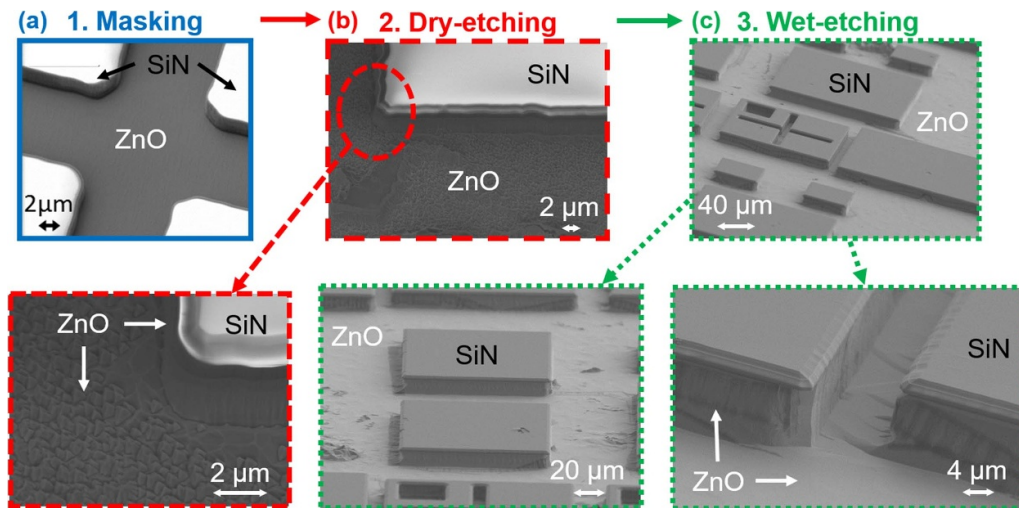


**Figure 3.** SEM images of the three-step etching procedure: (a) masking and patterning: with/of SiN, (b) dry-etching: in CH<sub>4</sub>-based chemistry and (c) wet-etching: in diluted HCl for surface defect and sidewall curing and smoothing.

**Table 2.** Values of the etch-rate selectivity between ZnO (substrate or doped MBE layer) and ZnMgO for two dilutions of HCl. The highest selectivity results in a ratio of  $\sim 5$  (etching substrate and dilution of 1:16 in H<sub>2</sub>O).

HCl dilution ratio HCl:H <sub>2</sub> O	Selectivity	
	ZnO <sub>substrate</sub> /ZnMgO	ZnO <sub>doped MBE</sub> /ZnMgO
1:4	1.5	2.2
1:16	5.2	3.9

The quality of the layer/substrate might be the origin, of why the two ZnO samples (substrate and epitaxial layer) have different etch-rates [70], together with some impact of the doping-level on the etch rate.

It is worth noting, that, the etch-rate for ZnMgO is a function of the Mg-content. Consequently, a higher Mg-content yields even slower etch-rates as seen for our methane-based process. At the same time, the maximum layer thickness that can be grown in this case is limited by built-in strain (see section 8.5 in the supplementary material).

#### 4. Suppression of ICP-etching induced surface leakage currents

Surface currents are a known leakage mechanism for electrons in various compound semiconductors [1, 2] including the wide gap semiconductors GaN [3] and ZnO [78]. While those currents and their enhancement by additional plasma treatment of the semiconductor surface, can result in a further reduced resistivity, which is beneficial e.g. for better n-type ohmic contacts in ZnO devices [79], they still pose a parasitic loss mechanism for etched semiconductors or more complex structures like heterostructures. In particular, the treatment in an Ar- and/or Hydrogen-ICP plasma reduces the specific contact resistivity of ZnO-based structures up to more than two orders of magnitude [79] and can be explained by the bombardment of the sample surface with high energy argon/hydrogen ions (see section 8.6). Unfortunately, the ICP-etching of our m-Zn(Mg)O samples also uses

those two surface-conductivity enhancing gasses (Ar and H<sub>2</sub>). Moreover our etching recipe shows similarities to another reported etching procedure by Lee *et al* which was used for enhancing n-type contacts on ZnO (cp. section 8.6 and [79]), i.e. basically the opposite of what we want to achieve by suppressing those surface currents. In addition, CH<sub>4</sub>-based etching tends to incorporate carbon in the Zn(Mg)O surface [68], which can act as a n-dopant and consequently also further enhance surface leakage currents [80, 81] (see also section 8.6).

In order to obtain proper device operation for our samples, we have to counteract all the previously mentioned effects and suppress such surface leakage currents efficiently. This can e.g. be achieved by introducing a highly-resistive ‘Shottky-contact-like’ layer on top of the Zn(Mg)O, e.g. through treatment with H<sub>2</sub>O<sub>2</sub>. In that case hydrogen peroxide forms a highly resistive, O<sub>2</sub>-rich surface layer on top of the ZnO, which results in an upward bending of the energy band at the sample surface [78]. Another positive effect of the H<sub>2</sub>O<sub>2</sub> treatment is the reduction of deep-level defects in ZnO through the reaction of the ZnO surface with O<sub>2</sub>-radicals, resulting in a reduced net-carrier concentration at the sample surface and hence surface leakage current suppression by several orders of magnitude [82]. For more details on the processes and mechanisms of surface leakage current suppression through the application of H<sub>2</sub>O<sub>2</sub> to ZnO, please see section 8.6 of the supplementary material.

In addition to a H<sub>2</sub>O<sub>2</sub> treatment, we also tested exposing our m-ZnO samples to a strong oxygen plasma in order to

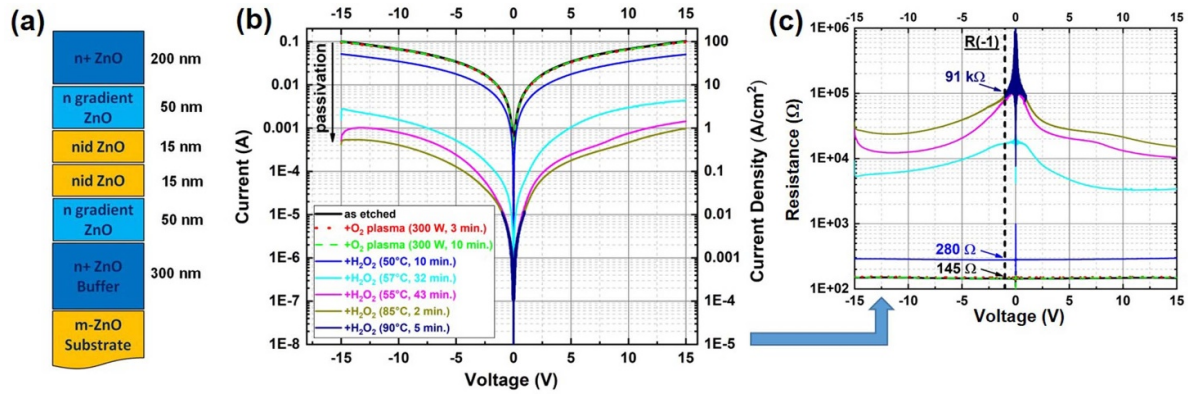


**Figure 4.** (a) Layer sequence of the passivation-test sample. (b) IV-characteristics of the  $\text{CH}_4/\text{Ar}/\text{H}_2$  etched m-plane ZnO test samples (logarithmic-scale) as etched and under  $\text{O}_2$ -plasma and  $\text{H}_2\text{O}_2$ -treatment for different temperatures and exposure times. (c) Resulting voltage-dependent resistance after surface treatment.

obtain an oxygen-rich and therefore resistive surface layer. We tested the treatments on etched square Mesas ( $\text{CH}_4$ -based etching presented in section 3.4) in a layer sequence as shown in figure 4(a). It consists of a 30 nm thick non-intentionally doped ZnO layer sandwiched between doped ZnO contact layers and 10/200 nm thick Ti/Au metal contacts. Figure 4(b) shows the IV-characteristics of the sample in a logarithmic plot. We extract an ohmic behavior with a resistance of 145  $\Omega$  at  $-1$  V (black line) for the as-etched sample (see figure 4(c)).

While treating the sample in an  $\text{O}_2$ -plasma in two successive steps, i.e. 300 W and 3 min followed by 300 W and 10 min (red and green line in figures 4(b) and (c), respectively) has basically no effect on the IV-curve and resistance at all, exposing it to  $\text{H}_2\text{O}_2$  (32%) in a third step for 10 min at 50  $^\circ\text{C}$  almost doubles the (still ohmic, i.e. constant) resistance to 280  $\Omega$  at  $-1$  V. This also means, that the current passing through the Mesa is reduced to half of its initial value. Another exposure, this time at 57  $^\circ\text{C}$  for 32 min, yields a much larger reduction of the current by about two orders of magnitude to currents in the mid- $10^{-2}$  Milliampere range. This is accompanied by a change of the resistive behavior to a Schottky-like resistance (see asymmetry in figures 4(b) and non-constant curves in (c)). As expected, additional treatments in hydrogen peroxide at even higher temperatures (e.g. 85  $^\circ\text{C}$  and 90  $^\circ\text{C}$ ) can be performed at much shorter times (e.g. 2 and 5 min), while still further reducing the measured current. We measure the highest resistance after the 5 min 90  $^\circ\text{C}$   $\text{H}_2\text{O}_2$  treatment (91 k $\Omega$  at  $-1$  V), which is similar to the results of e.g. [83], who fabricated Au/n-ZnO rectifying contacts with such a treatment (more details given in section 8.6 of the supplementary material).

In order to reduce the needed total exposure time, we use 95  $^\circ\text{C}$  for 5 min as standard procedure for all following samples, yielding similar surface leakage current suppression as the results shown in figures 4(b) and (c). In agreement with [83], we also observe a significant surface roughening at 100  $^\circ\text{C}$  ( $\geq 1$  min), identified through a change of the surface investigated with a microscope from a shiny yellow color to a dim brown one.

## 5. Conclusion

In conclusion, we investigated different etching schemes for (non-polar) m-Zn(Mg)O epitaxial layers on m-plane ZnO substrates, including various wet chemical and ICP-RIE dry etching recipes. While solely applying dry etching in a  $\text{CH}_4$ -based chemistry results in vertical sidewalls with decent etch-rates (0.5–0.8 nm  $\text{s}^{-1}$ ) and good selectivity towards a PECVD-deposited SiN mask ( $\sim 1:10$ ), it leaves ‘grass-like’ residuals on the etched surface. In contrast to that, wet chemical etching, e.g. in diluted HCl or  $\text{H}_3\text{PO}_4$ , shows high etch rates ( $\sim 20$ –90 nm  $\text{s}^{-1}$ ) and selectivity towards an Au or SiN mask, but with significant undercut.

The best way to mitigate the drawbacks of both techniques, is in combining them: first dry etching to define the profile and etch the major part of the structure, followed by a smoothing etch in diluted (1:16) HCl to remove the residuals and defects from the ion bombardment and the different Zn- and O- etch rates at the sample surface during ICP-RIE etching. In addition to that, subsequently exposing the sample to  $\text{H}_2\text{O}_2$  for  $\sim 5$  min at 95  $^\circ\text{C}$  reduces surface leakage currents from the plasma-based etching by more than two orders of magnitude. Similar effects of leakage current suppression could be identified for samples containing a significant amount of Mg in their ZnMgO layers, i.e. by increasing the barrier height of the quantum wells (cp. also [84]). This could e.g. be observed by fabricating QCD structures with 20 periods in their active region [51] and will be the topic of future investigations.

One additional advantage of using HCl is its observed selectivity between ZnO and ZnMgO etching (up to  $\sim 1:4$  to 1:5), allowing the latter to be used as ‘etch-stop’ layer in double metal waveguides, often used for THz QCL devices.

## Acknowledgments

The authors want to acknowledge expert technical assistance for sample growth, optical and AFM characterization by Denis Lefebvre, Nolwenn Le Biavan and Daniela Ristanic. This work was supported financially by the European Union’s

Horizon 2020 Research and Innovation FET-Open Program through the project ‘ZOTERAC’ under Grant Agreement No. 665107. The authors acknowledge TU Wien Bibliothek for financial support through its Open Access Funding Program.

## ORCID iDs

Borislav Hinkov  <https://orcid.org/0000-0003-2564-5449>

Hanh T Hoang  <https://orcid.org/0000-0001-8095-3650>

Gottfried Strasser  <https://orcid.org/0000-0003-0147-0883>

## References

- [1] Sidor D E, Savich G R and Wicks G W 2016 Surface leakage mechanisms in III–V infrared barrier detectors *J. Electron. Mater.* **45** 4663–7
- [2] Ma Y *et al* 2016 Impact of etching on the surface leakage generation in mesa-type InGaAs/InAlAs avalanche photodetectors *Opt. Express* **24** 7823
- [3] Zhang H, Jacopin G, Neplokh V, Largeau L, Julien F H, Kryliouk O and Tchernycheva M 2015 Color control of nanowire InGaN/GaN light emitting diodes by post-growth treatment *Nanotechnology* **26** 465203
- [4] Kim S M *et al* 2006 Biomedical terahertz imaging with a quantum cascade laser *Appl. Phys. Lett.* **88** 1–3
- [5] Bartalini S *et al* 2014 Frequency-comb-assisted terahertz quantum cascade laser spectroscopy *Phys. Rev. X* **4** 021006
- [6] Patimisco P, Scamarcio G, Tittel F K and Spagnolo V 2014 Quartz-enhanced photoacoustic spectroscopy: a review *Sensors* **14** 6165–206
- [7] Darmo J *et al* 2004 Imaging with a terahertz quantum cascade laser *Opt. Express* **12** 1879–84
- [8] Dean P *et al* 2014 Terahertz imaging using quantum cascade lasers—a review of systems and applications *J. Phys. D: Appl. Phys.* **47** 374008
- [9] Nakanishi A, Fujita K, Horita K and Takahashi H 2019 Terahertz imaging with room-temperature terahertz difference-frequency quantum-cascade laser sources *Opt. Express* **27** 1884–93
- [10] Zhang J, Mikulics M, Serafini J, Gong M, Adam R, Grützmacher D and Sobolewski R 2011 Ultrafast GaAs nano-whisker photodetector for THz-frequency applications *CLEO:2011 - Laser Applications to Photonic Applications* (Washington, DC: Optical Society of America) **JTu119**
- [11] NASA Stratospheric Observatory for Infrared Astronomy (SOFIA) ([www.nasa.gov/mission\\_pages/SOFIA/](http://www.nasa.gov/mission_pages/SOFIA/))
- [12] Hübers H W, Richter H and Wienold M 2019 High-resolution terahertz spectroscopy with quantum-cascade lasers *J. Appl. Phys.* **125** 151401
- [13] Behnken B N, Karunasiri G, Chamberlin D R, Robrish P R and Faist J 2008 Real-time imaging using a 2.8 THz quantum cascade laser and uncooled infrared microbolometer camera *Opt. Lett.* **33** 440–2
- [14] Köhler R, Tredicucci A, Beltram F, Beere H E, Linfield E H, Davies A G, Ritchie D A, Iotti R C and Rossi F 2002 Terahertz semiconductor-heterostructure laser *Nature* **417** 156–9
- [15] Kainz M A *et al* 2019 Thermoelectric-cooled terahertz quantum cascade lasers *Opt. Express* **27** 20688–93
- [16] Bosco L, Franckí M, Scalari G, Beck M, Wacker A and Faist J 2019 Thermoelectrically cooled THz quantum cascade laser operating up to 210 K *Appl. Phys. Lett.* **115** 010601
- [17] Faist J, Sirtori C, Capasso F, Pfeiffer L and West K W 1994 Phonon limited intersubband lifetimes and linewidths in a two-dimensional electron gas *Appl. Phys. Lett.* **64** 872–4
- [18] Faist J 2013 *Quantum Cascade Lasers* (Oxford: Oxford University Press) ch 5 (<https://doi.org/10.1093/acprof:oso/9780198528241.001.0001>)
- [19] Brandstetter M *et al* 2016 InAs based terahertz quantum cascade lasers *Appl. Phys. Lett.* **108** 011109
- [20] Ajili L, Scalari G, Hoyler N, Giovannini M and Faist J 2005 InGaAs–AlInAs/InP terahertz quantum cascade laser *Appl. Phys. Lett.* **87** 141107
- [21] Fischer M, Scalari G, Walther C and Faist J 2009 Terahertz quantum cascade lasers based on In<sub>0.53</sub>Ga<sub>0.47</sub>As/In<sub>0.52</sub>Al<sub>0.48</sub>As/InP *J. Cryst. Growth* **311** 1939–43
- [22] Deutsch C *et al* 2017 High-power growth-robust InGaAs/InAlAs terahertz quantum cascade lasers *ACS Photonics* **4** 957–62
- [23] Terashima W and Hirayama H 2015 GaN-based terahertz quantum cascade lasers *Proc. SPIE* **9483** 948304
- [24] Ahi K 2017 Review of GaN-based devices for terahertz operation *Opt. Eng.* **56** 090901
- [25] Stradling R A and Wood R A 1970 The temperature dependence of the band-edge effective masses of InSb, InAs and GaAs as deduced from magnetophonon magnetoresistance measurements *J. Phys. C: Solid State Phys.* **3** L94
- [26] Shantharama L G, Adams A R, Ahmad C N and Nicholas R J 1984 The kp interaction in InP and GaAs from the band-gap dependence of the effective mass *J. Phys. C: Solid State Phys.* **17** 4429–42
- [27] Valmorra F, Scalari G, Ohtani K, Beck M and Faist J 2015 InGaAs / AlInGaAs THz quantum cascade lasers operating up to 195 K in strong magnetic field *New J. Phys.* **17** 023050
- [28] Preisler V, Ferreira R, Hameau S, De Vaulchier L A, Guldner Y, Sadowski M L and Lemaitre A 2005 Hole-LO phonon interaction in InAs/GaAs quantum dots *Phys. Rev. B* **72** 1–6
- [29] Mooradian A and Wright G B 1966 First order Raman effect in III-V compounds *Solid State Commun.* **4** 431–4
- [30] Dubajić M, Daničić A, Vuković N, Milanović V and Radovanović J 2018 Optimization of cubic GaN/AlGaIn quantum cascade structures for negative refraction in the THz spectral range *Opt. Quantum Electron.* **50** 1–10
- [31] Li J, Wan T and Chen C 2019 Two-phonon-resonance terahertz quantum cascade laser based on GaN/AlGaIn material system *Semicond. Sci. Technol.* **34** 075018
- [32] Bellotti E, Driscoll K, Moustakas T D and Paiella R 2009 Monte Carlo simulation of terahertz quantum cascade laser structures based on wide-bandgap semiconductors *J. Appl. Phys.* **105** 113103
- [33] Borysiewicz M A 2019 ZnO as a functional material, a review *Crystals* **9** 505
- [34] Moezzi A, McDonagh A M and Cortie M B 2012 Zinc oxide particles: synthesis, properties and applications *Chem. Eng. J.* **185**–6 1–22
- [35] Lafrentz M, Brunne D, Rodina A V, Pavlov V V, Pisarev R V, Yakovlev D R, Bakin A and Bayer M 2013 Second-harmonic generation spectroscopy of excitons in ZnO *Phys. Rev. B* **88** 235207
- [36] Zhu J, Emanetoglu N W, Chen Y, Yakshinskiy B V and Lu Y 2004 Wet-chemical etching of (1120) ZnO films *J. Electron. Mater.* **33** 556–9
- [37] Martinson A B, Elam J W, Hupp J T and Pellin M J 2007 ZnO nanotube based dye-sensitized solar cells *Nano Lett.* **7** 2183–7
- [38] Cheng Y *et al* 2017 Role of defects and surface states in the carrier transport and nonlinearity of the diode characteristics in PbS/ZnO quantum dot solar cells *Appl. Mater. Interfaces* **9** 13269–77
- [39] Subramanian V, Bakhishev T, Redinger D and Volkman S K 2009 Solution-processed zinc oxide transistors for low-cost electronics applications *IEEE/OSA J. Disp. Technol.* **5** 525–30

- [40] Sadek A Z, Choopun S, Wlodarski W, Ippolito S J and Kalantar-zadeh K 2007 Characterization of ZnO nanobelt-based gas sensor for H<sub>2</sub>, NO<sub>2</sub> and hydrocarbon sensing *IEEE Sens. J.* **7** 919–24
- [41] Mehta M and Meier C 2011 Controlled etching behavior of O-polar and Zn-polar ZnO single crystals *J. Electrochem. Soc.* **158** H119
- [42] Gopal P and Spaldin N A 2006 Polarization, piezoelectric constants and elastic constants of ZnO, MgO and CdO *J. Electron. Mater.* **35** 538–42
- [43] Yang J, Wang J, Li X, Lang J, Liu F, Yang L, Zhai H, Gao M and Zhao X 2012 Effect of polar and non-polar surfaces of ZnO nanostructures on photocatalytic properties *J. Alloys Compd.* **528** 28–33
- [44] Izyumskaya N, Tahira A, Ibupoto Z H, Lewinski N, Avrutin V, Özgür U, Topsakal E, Willander M and Morkoç H 2017 Review—electrochemical biosensors based on ZnO nanostructures *ECS J. Solid State Sci. Technol.* **6** Q84–100
- [45] Meyer B and Marx D 2003 Density-functional study of the structure and stability of ZnO surfaces *Phys. Rev. B* **67** 035403
- [46] Li G R, Hu T, Pan G L, Yan T Y, Gao X P and Zhu H Y 2008 Morphology-function relationship of ZnO: polar planes, oxygen vacancies and activity *J. Phys. Chem C* **112** 11859–64
- [47] Tainoff D, Al-Khalifou M, Deparis C, Vinter B, Teisseire M, Morhain C and Chauveau J M 2011 Residual and nitrogen doping of homoepitaxial nonpolar m-plane ZnO films grown by molecular beam epitaxy *Appl. Phys. Lett.* **98** 131915
- [48] Tabares G, Hierro A, Lopez-Ponce M, Muñoz E, Vinter B and Chauveau J M 2015 Light polarization sensitive photodetectors with m- and r-plane homoepitaxial ZnO/ZnMgO quantum wells *Appl. Phys. Lett.* **106** 061114
- [49] Le Biavan N et al 2017 Homoepitaxy of non-polar ZnO/(Zn,Mg)O multi-quantum wells: from a precise growth control to the observation of intersubband transitions *Appl. Phys. Lett.* **111** 231903
- [50] Montes Bajo M et al 2018 Multisubband plasmons in doped ZnO quantum wells *Phys. Rev. Appl.* **10** 024005
- [51] Jollivet A et al 2018 Short infrared wavelength quantum cascade detectors based on m-plane ZnO / ZnMgO quantum wells *Appl. Phys. Lett.* **113** 251104
- [52] Giofrè M, Gagliardi M, Casalino M, Coppola G, Iodice M and Della Corte F 2007 Fabrication and characterization of zinc oxide based rib waveguide *Proc. SPIE* **6474** 64741H
- [53] Yen W T, Lin Y C and Ke J H 2010 Surface textured ZnO:Al thin films by pulsed DC magnetron sputtering for thin film solar cells applications *Appl. Surf. Sci.* **257** 960–8
- [54] Kozuka Y, Tsukazaki A and Kawasaki M 2014 Challenges and opportunities of ZnO-related single crystalline heterostructures *Appl. Phys. Rev.* **1** 011303
- [55] Valtiner M, Torrelles X, Pareek A, Borodin S, Gies H and Grundmeier G 2010 In situ study of the polar ZnO(0001)-Zn surface in alkaline electrolytes *J. Phys. Chem. C* **114** 15440–7
- [56] Nicholas N J, Ducker W and Franks G V 2012 Differential etching of ZnO native planes under basic conditions *Langmuir* **28** 5633–41
- [57] Lin W H, Saito H, Nemoto T, Kurata H, Chou M M C, Isoda S and Wu J J 2012 Photoassisted scanning tunneling microscopy investigation on the ZnO(0001)-Zn surface treated by alkaline solution *J. Phys. Chem. C* **116** 10664–71
- [58] Suzuki S, Miyata T, Ishii M and Minami T 2003 Transparent conducting V-co-doped AZO thin films prepared by magnetron sputtering *Thin Solid Films* **434** 14–19
- [59] Shin K S, Park H J, Kumar B, Kim K H, Kim S H and Kim S W 2012 Inverted organic solar cells with ZnO nanowalls prepared using wet chemical etching in a KOH solution *J. Nanosci. Nanotechnol.* **12** 1234–7
- [60] Zhu J, Saraf G, Zhong J, Sheng H F, Yakshinskiy B V and Lu Y 2006 SiCl<sub>4</sub>-based reactive ion etching of ZnO and Mg<sub>x</sub>Zn<sub>1-x</sub>O films on r-sapphire substrates *J. Electron. Mater.* **35** 1311–5
- [61] Pearton S J, Chen J J, Lim W T, Ren F and Norton D P 2007 Wet chemical etching of wide bandgap semiconductors-GaN, ZnO and SiC *ECS Trans.* **6** 501–12
- [62] Kim D, Hwang I, Son J and Kim H 2011 Inductively coupled-plasma dry etching of a ZnO thin film by Ar-diluted CF<sub>4</sub> gas *J. Korean Phys. Soc.* **58** 1536–40
- [63] Lee J-M, Chang K-M, Kim K-K, Choi W-K and Park S-J 2001 Dry etching of ZnO using an inductively coupled plasma *J. Electrochem. Soc.* **148** G1
- [64] Pearton S, Norton D, Ip K, Heo Y and Steiner T 2003 Recent progress in processing and properties of ZnO *Superlattices Microstruct.* **34** 3–32
- [65] Na S W, Shin M H, Chung Y M, Han J G, Jeung S H, Boo J H and Lee N E 2006 Etching characteristics of ZnO thin films in chlorine-containing inductively coupled plasmas *Microelectron. Eng.* **83** 328–35
- [66] Chang S-C, Hicks D B and Laugel R C O 1992 Patterning of zinc oxide thin films *IEEE Solid-State Sensor and Actuator Workshop* (Piscataway, NJ: IEEE) pp 41–5
- [67] Mastropaolo E, Gundlach A M, Fragkiadakis C, Kirby P B and Cheung R 2007 Reactive ion etching of zinc oxide (ZnO) in SiCl<sub>4</sub> based plasmas *Electron. Lett.* **43** 1467–9
- [68] Na S-W, Shin M H, Chung Y M, Han J G and Lee N-E 2005 Investigation of process window during dry etching of ZnO thin films by CH<sub>4</sub>-H<sub>2</sub>-Ar inductively coupled plasma *J. Vac. Sci. Technol. A* **23** 898
- [69] Lee K K, Luo Y, Lu X F, Bao P and Song A M 2011 Development of reactive-ion etching for ZnO-based nanodevices *IEEE Trans. Nanotechnol.* **10** 839–43
- [70] Mehta M, Ruth M, Piegdon K A, Krix D, Nienhaus H and Meier C 2009 Inductively coupled plasma reactive ion etching of bulk ZnO single crystal and molecular beam epitaxy grown ZnO films *J. Vac. Sci. Technol. B* **27** 2097–101
- [71] Guo Q, Uesugi N, Tanaka T, Nishio M and Ogawa H 2006 Reactive ion etching of zinc oxide using methane and hydrogen *Japan. J. Appl. Phys.* **1** **45** 8597–99
- [72] Hsueh K-P, Hou R-J, Kuo C-H and Tun C-J 2008 Reactive ion etching of ZnO using the H<sub>2</sub>/CH<sub>4</sub> and H<sub>2</sub>/CH<sub>4</sub>/AR mixtures *Optoelectron. Mater. Devices* **7135** 71350D
- [73] Faist J 2013 *Quantum Cascade Lasers* (Oxford: Oxford University Press) ch 9 (<https://doi.org/10.1093/acprof:oso/9780198528241.001.0001>)
- [74] Bismuto A 2011 Mid-infrared quantum cascade lasers: active medium and waveguide engineering *PhD Thesis* ETH Zürich (<https://doi.org/10.3929/ethz-a-006716259>)
- [75] Williams B S, Kumar S, Callebaut H, Hu Q and Reno J L 2003 Terahertz quantum-cascade laser at  $\lambda = 100 \mu\text{m}$  using metal waveguide for mode confinement *Appl. Phys. Lett.* **83** 2124–6
- [76] Kim J H, Jung S, Jiang Y, Fujita K, Hitaka M, Ito A, Edamura T and Belkin M A 2018 Double-metal waveguide terahertz difference-frequency generation quantum cascade lasers with surface grating outcouplers *Appl. Phys. Lett.* **113** 161102
- [77] Martl M, Darmo J, Deutsch C, Brandstetter M, Andrews A M, Klang P, Strasser G and Unterrainer K 2011 Gain and losses in THz quantum cascade laser with metal-metal waveguide *Opt. Express* **19** 733

- [78] Schifano R, Monakhov E V, Svensson B G and Diplas S 2009 Surface passivation and interface reactions induced by hydrogen peroxide treatment of n-type ZnO *Appl. Phys. Lett.* **94** 132101
- [79] Lee J M, Kim K K, Park S J and Choi W K 2001 Low-resistance and nonalloyed ohmic contacts to plasma treated ZnO *Appl. Phys. Lett.* **78** 3842–4
- [80] Park J W, Kim D H, Choi S H, Lee M and Lim D 2010 The role of carbon doping in ZnO *J. Korean Phys. Soc.* **57** 1482–5
- [81] Zhang X, Qin J, Hao R, Wang L, Shen X, Yu R, Limpanart S, Ma M and Liu R 2015 Carbon-doped ZnO nanostructures: facile synthesis and visible light photocatalytic applications *J. Phys. Chem C* **119** 20544–54
- [82] Kim S H, Kim H K and Seong T Y 2005 Effect of hydrogen peroxide treatment on the characteristics of Pt Schottky contact on n-type ZnO *Appl. Phys. Lett.* **86** 1–3
- [83] Gu Q L *et al* 2008 Au/n-ZnO rectifying contact fabricated with hydrogen peroxide pretreatment *J. Appl. Phys.* **103** 093706
- [84] Sakr S, Kotsar Y, Tchernycheva M, Warde E, Isac N, Monroy E and Julien F H 2012 Resonant tunneling transport in a GaN/AlN multiple-quantum-well structure *Appl. Phys. Express* **5** 052203